

A discrete element model for the development of compaction localization in granular rock

Baoshan Wang,¹ Yong Chen,¹ and Teng-fong Wong²

Received 13 May 2006; revised 16 September 2007; accepted 13 December 2007; published 11 March 2008.

[1] A discrete element model was developed to simulate the micromechanics of compaction localization in a granular rock. The rock was modeled as a bonded assembly of circular disks, and seven different distributions of radius were considered. To simulate grain crushing and pore collapse, an intragranular damage mechanism was introduced that allows for the shrinkage of a disk if one of its normal contact stresses attains a critical value. The model captures key attributes of failure mode and damage evolution associated with the brittle-ductile transition in porous sandstones. Our simulations indicate that the development of discrete compaction bands is promoted in a relatively homogeneous granular aggregate, while diffuse band growth and distributed cataclastic flow are preferred modes of compaction in a more heterogeneous system. To interpret the former result an Eshelby inclusion model was proposed to estimate analytically the local stress perturbations due to pore collapse in a homogeneous aggregate.

Citation: Wang, B., Y. Chen, and T.-f. Wong (2008), A discrete element model for the development of compaction localization in granular rock, *J. Geophys. Res.*, 113, B03202, doi:10.1029/2006JB004501.

1. Introduction

[2] Since strain localization as a failure mode can significantly influence the stress field, strain partitioning and fluid transport in many tectonic settings, it is important to have a fundamental understanding of the mechanics of this phenomenon. In clastic rocks failure typically localizes along deformation bands, which are tabular zones of concentrated strain that may be in shear, compaction or dilation [Aydin, 1978; Aydin *et al.*, 2006]. A kinematic end-member of such strain localization is represented by compaction bands, which are planar structures that have undergone inelastic compaction predominately due to shortening in a direction subperpendicular to their planar surfaces with negligible shear offset. In a seminal study Mollema and Antonellini [1996] demonstrated that the significant porosity reduction observed within compaction bands had derived from relative grain movement and microcracking, with minimal contribution from diffusive mass transfer processes such as pressure solution. Their field area was in the Kalibab monocline, Utah where compaction bands in the Jurassic Navajo sandstone were observed to have trace lengths of several meters, comparable to those previously measured by Hill [1989] in the Jurassic Aztec sandstone in the Valley of Fire State Park, Nevada. Recently Sternlof *et al.* [2005] have revisited the Valley of Fire site, where they documented extensive arrays of subparallel compaction bands that extend up to tens of meters.

[3] In the laboratory, the development of compaction localization has recently been investigated in sandstones with porosities ranging from 13% to 28% [Olsson and Holcomb, 2000; DiGiovanni *et al.*, 2000; Klein *et al.*, 2001]. The data show that localized failure in a compactant rock is commonly associated with stress states in the transitional regime from brittle faulting to cataclastic flow [Wong *et al.*, 2001], with mode of localization associated with a broad spectrum of geometric complexity [Baud *et al.*, 2004]. Two end-members of failure mode have been observed in the most porous and compact sandstones, respectively: arrays of discrete compaction bands subperpendicular to the maximum compression (σ_1) direction, and shear bands at relatively high angles to σ_1 . In sandstones with intermediate porosities, a hybrid localization mode involving high-angle shear bands and diffuse compaction bands was observed. Different compaction localization modes are manifested by distinct acoustic emission (AE) signatures, and microstructural observations show intense grain crushing and pore collapse inside the compaction bands. Significant reductions of permeability have also been observed while a sample undergoes compaction localization [Holcomb and Olsson, 2003; Vajdova *et al.*, 2004a].

[4] Important insight into the mechanics of compaction localization has been gained from the continuum analysis of its inception as a bifurcation in the constitutive response of a porous medium [Olsson, 1999]. Critical conditions for the onset of localization and orientations of high-angle shear and compaction bands can be derived as functions of the constitutive parameters [Issen and Rudnicki, 2000; Issen, 2002; Rudnicki, 2004.]. While bifurcation analysis provides a very useful framework for understanding compaction localization, it has an intrinsic limitation in that the continuum analysis addresses only the onset of constitutive

¹Institute of Geophysics, China Earthquake Administration, Beijing, China.

²Department of Geosciences, Stony Brook University, New York, USA.

instability in an initially homogeneous material, but not the subsequent propagation behavior of the localization structures or development of their geometric complexities. In particular, this continuum approach cannot explain why compaction bands preferentially develop as an array of many discrete bands or as one or two diffuse structures that widen laterally. These differences have been attributed to microstructural heterogeneities which are difficult to capture in a continuum model [Katsman *et al.*, 2005]. Klein *et al.* [2001] speculated that discrete compaction bands are predominant in the Bentheim sandstone possibly due to its relatively homogeneous mineralogy (with 95% quartz, 3% orthoclase and 3% kaolinite) and well-sorted grains. In contrast Olsson and Holcomb [2000] observed diffuse compaction bands in the Castlegate sandstone with 70–80% quartz and 5–10% clay. Baud *et al.* [2004] emphasized that, although in their study arrays of discrete compaction bands were observed only in the Bentheim and Diemelstadt sandstones with the highest porosities (23% and 24%, respectively), porosity cannot be the only microstructural attribute that promotes the development of discrete bands, since diffuse and not discrete bands develop in Castlegate sandstone which has an initial porosity of 28% that is higher than all five sandstones they investigated.

[5] To address some of these questions related to how grain-scale heterogeneity influences the development of strain localization, it is necessary to consider a micromechanical model accounting for the heterogeneity. The discrete element (DE) method has proved to be an effective tool for simulating the micromechanics of failure in unconsolidated materials, such as soil, sediment and fault gouge [e.g., Cundall and Strack, 1979; Antonellini and Pollard, 1995; Mora and Place, 1998; Morgan and Boettcher, 1999; Aharonov and Sparks, 2002; Hazzard and Mair, 2003]. In a DE model local deformation on the grain scale can arise from elastic strains at impinging grain contacts or relative slip among grains, which collectively contribute to a global strain field in the granular assembly that may be homogeneously distributed or localized. The method has been extended to a bonded granular material [Potyondy *et al.*, 1996; Potyondy and Cundall, 2004], with contacts that can be bonded and thus unable to slip. Typically such a contact is assigned a tensile and shear strength, and if either of these stress thresholds is attained the bond would rupture, thus opening the possibility for relative slip between neighboring grains when the local tangential force is sufficiently high to overcome the frictional resistance at the ruptured grain contact. Such an approach has been adopted to model the micromechanics of failure [Hazzard *et al.*, 2000], AE activity [Hazzard and Young, 2002] and sonic velocities [Hazzard and Young, 2004] of a cohesive rock. Notwithstanding the success of these DE models in capturing the micromechanics of failure, there is a limitation in that they do not explicitly account for intragranular damage. In relation to the compactive failure of elastic rocks, microstructural observations have revealed pervasive Hertzian cracking that initiates from impinging grain contacts, which ultimately leads to grain crushing and pore collapse [Zhang *et al.*, 1990; Menéndez *et al.*, 1996]. The spatial clustering of such damage results in compaction localization manifested by characteristic AE signatures [Baud *et al.*, 2004].

[6] In this study we develop a 2-dimensional DE model to simulate the micromechanics of failure in a porous sandstone with several questions in mind. How can grain crushing and pore collapse be incorporated in a DE model? To what extent can such a model simulate the inelastic behavior and failure modes associated with the brittle-ductile transition? Can such simulations provide insights into how grain-scale heterogeneity influences the AE activity and geometric complexity of compaction localization? The porous sandstone is modeled as a bonded assembly of circular disks, with different distributions of radius. An intragranular damage mechanism is introduced that allows for the shrinkage of a disk if one of its normal contact stresses attains a critical value.

2. Numerical Model

[7] For our numerical simulations we used the Particle Flow Code (PFC^{2D}) developed by Itasca Consulting Group, a DE modeling package that considers the rock as a bonded assemblage of circular disks and analyzes the internal deformation by solving the equations of motion using a time stepping, explicit scheme [Potyondy and Cundall, 2004]. Except for the consideration of intragranular damage and disk shrinkage, our simulations follow closely the numerical methodology of Hazzard *et al.* [2000], who provided a detailed description of principles and assumptions related to the Particle Flow Code.

[8] The disks are assumed to be rigid, so deformation can occur only at point contacts between neighboring disks. At such a point the contact force \vec{F} is assumed to be linearly related to the relative displacement $\vec{\delta}$ between the centers of the two contacting disks, so that local deformation can be characterized by a normal stiffness K_n and shear stiffness K_s . Initially all the contacts are bonded. A contact bond can withstand extensile and shear deformation, but when the magnitude of the normal force F_n attains a threshold value S_n in tension the bond breaks and instantaneously \vec{F} vanishes. Similarly the bond may break when the tangential force F_t attains a threshold value of S_n , but in this case the force would not vanish but drop to a residual value given by $F_t = \mu F_n$, where μ denotes the friction coefficient. This friction criterion also dictates whether two neighboring disks undergo relative slip at a contact with broken bond.

2.1. Intragranular Damage and Pore Collapse

[9] In addition to these two damage mechanisms involving tensile and shear failure at intergranular contacts, our DE model incorporates a third mechanism that simulates intragranular damage leading to grain crushing and pore collapse. To our knowledge two different approaches have been proposed for this mechanism. Li and Holt [2002] and Boutt and McPherson [2002] modeled the rock as an assemblage of “superparticles” made up of clusters of bonded particles. The bond strength at a contact between particles within a cluster is assumed to be higher than that at a contact between superparticles, so that “intragranular” damage may develop inside a cluster if loading continues to increase after most of the “intergranular” cluster bonds have ruptured. Breakage of bonds inside a superparticle mimics grain crushing, and the relative movement of particles within the cluster contributes to pore collapse.

Table 1. Micromechanical Parameters Used in DE Simulations

Parameter	Value
E_c	88 GPa
K_n/K_t	1
μ	0.5
Average value of τ_{cr} and σ_{cr}	100 MPa
Standard deviation of distributions of τ_{cr} and σ_{cr}	25 MPa
σ_{cr}^g	200 MPa

While this approach is quite versatile in reproducing modes of dilatant and compactive failure [Li and Holt, 2002], the simulations are sensitive to the exact manner in which the superparticles are clustered [Boutt and McPherson, 2002].

[10] A somewhat different approach was proposed by Bruno and Nelson [1991] in their DE model of compactive failure of sedimentary rocks, and by Couroyer *et al.* [2000] in their study of bulk crushing of porous alumina. The damage mechanism is modeled as extensile cracking that initiates when the normal contact forces induce a tensile stress concentration within the grain which exceeds its tensile strength σ_{cr}^g . Such a process is analogous to the “Brazilian test”, which develops extensile cracking within a circular disk of radius R when the normal force attains the critical value of $F_n = \pi R \sigma_{cr}^g$ [Jaeger and Cook, 1979]. In this study we adopted an identical criterion for the initiation of intragranular damage.

[11] In the original formulation of Bruno and Nelson [1991], all the bonds in contact with a grain that satisfies the “Brazilian test” criterion are instantaneously broken. In contrast a more drastic approach was taken by Couroyer *et al.* [2000] and recently Marketos and Bolton [2005] who removed not only the bonds but also the grain itself completely from the assemblage. However, microstructural observations on compacted samples of sandstone [Menéndez *et al.*, 1996; Wu *et al.*, 2000; Baud *et al.*, 2004] indicate an intermediate scenario. Grain crushing and pore collapse arise from the progressive development of several intragranular cracks emanating from grain contacts, and to instantaneously remove all the bonds or the grain seem to be an overly drastic model of the damage evolution. In this study we adapted an approach formulated by Katsman *et al.* [2005], who simulated porosity reduction in their triangular network model by shortening the bond length by a constant ratio. We model the intragranular cracking and grain crushing processes in a progressive manner, allowing grains to shrink incrementally while maintaining some of the bonds intact. Specifically, only the bond with normal stress equal to or in excess of the critical threshold is removed (assuming that it has not been broken previously by intergranular failure), while the grain radius is reduced concomitantly by an amount εR . Grain shrinkage can facilitate the transfer of excess compressive force from the critical bond to other intact bonds and surrounding grains. The maximum number of times that a particular grain can undergo shrinkage is denoted by N_{\max} . Guided by the “damage index” data of Menéndez *et al.* [1996] for Berea sandstone and our simulation results for the average coordination number (~ 4), we chose a value of $N_{\max} = 4$. Accordingly the maximum amount of shrinkage that the grain radius can undergo is $N_{\max} \varepsilon R$. To reproduce laboratory observations

of porous sandstones we typically used a value of ε on the order of 0.01 in simulations presented in this paper.

2.2. Micromechanical Parameters

[12] Dilatant and compactive failures in rocks arise from the complex interplay of microcracking and pore collapse. A DE model is capable of reproducing the spatial heterogeneity of deformation that arises from relative grain movement as well as the propagation and coalescence of damage. However, it has a limitation intrinsic to most micromechanical models in that the grain geometry is highly idealized. Nevertheless previous DE studies have demonstrated that if the micromechanical parameters are calibrated appropriately, the stress-strain behavior and failure mode can be simulated in reasonable agreement with laboratory and microstructural observations. Specifically for DE models of a bonded granular medium, Hazzard *et al.* [2000] and Boutt and McPherson [2002] have elucidated how the micromechanical parameters (for input into the DE model) influence the macroscopic responses simulated.

[13] The pertinent parameters include the normal and shear stiffness (K_n and K_s), tensile and shear strengths of the bonds (S_n and S_t), and frictional coefficient (μ). The stiffnesses influence primarily the elastic responses of the bonded assemblage. Specifically the Young’s modulus is sensitively dependent on the normal stiffness, and it can be shown from dimensional analysis [Margolin and Trent, 1990] that the macroscopic Young’s modulus $E \propto (1 - \phi)n_c K_n/t$, where ϕ is the (areal) porosity, n_c the coordination number, and t the thickness of the 2-dimensional assemblage. A similar relation (with the thickness t replaced by the radius R) can also be derived for an assemblage of spheres [Digby, 1981; Walton, 1987]. Since both ϕ and n_c do not vary greatly in most DE models a calibrated value of E can be obtained by primarily adjusting the input parameter $E_c = k_n/(2t)$. Assuming unit thickness ($t = 1$) Hazzard *et al.* [2000] used an E_c value of 100 GPa to simulate the Lac du Bonnet granite with $E = 65$ GPa.

[14] In general, the areal porosity of a 2-dimensional assembly of circular disks is significantly lower than the porosities that can be attained in its 3-dimensional counterpart. Accordingly 2-dimensional DE models typically employ areal porosity values that are smaller than the porosities of the rocks of interest. For the Ekofisk chalk with porosities ranging from 28% to 48% Hazzard *et al.* [2000] used areal porosities in the range of 22–38% in their models. Since compaction localization has been observed mostly in sandstones with porosities of 20% or higher [Olsson, 1999; Wong *et al.*, 2001; Baud *et al.*, 2004], we focused our simulations on 2-dimensional assemblies with areal porosities of $\sim 16\%$. Given this discrepancy in porosity values, it is unrealistic to try matching exactly the simulated elastic behavior with laboratory data since porosity has a strong influence on the elastic moduli. The elastic strains (and the Young’s modulus values) in our simulations are therefore lower than those for a sandstone with porosities of 20% or higher, but comparable to those for a relatively compact sandstone with porosities of 15% or so (such as the Darley Dale sandstone [Wong *et al.*, 1997]). A value of $E_c = 88$ GPa was adopted in this study (Table 1).

[15] Observing that ratio of the normal to shear stiffness influences the Poisson’s ratio and that the friction coeffi-

Table 2. Radius Distributions in 7 Different Samples

Sample	R5r1	R45r12	R4r15	R33r2	R25r3	R2r3	R15r3
R_{\min} (mm)	0.50	0.45	0.40	0.33	0.25	0.20	0.15
R_{\max} (mm)	0.50	0.54	0.60	0.66	0.75	0.60	0.45
\bar{R} (mm)	0.5014	0.4935	0.4953	0.4846	0.4797	0.3838	0.2882
Number of grains	3866	3944	3866	3944	4774	6042	10741

cient μ controls the slope of the Mohr-Coulomb failure envelope, *Boutt and McPherson* [2002] arrived at values of $K_n/K_t = 1$ and $\mu = 0.5$ from their calibrations of sandstones and mudstones. We adopted the same values in this study (Table 1). It should be noted that *Hazzard et al.* [2000] used a higher friction coefficient of 0.7 to simulate the Lac du Bonnet and Westerly granites, and a lower value of 0.5 for the Ekofisk chalk which is highly porous and ductile.

[16] Typically in the PFC^{2D} code, bond strength is assumed to follow a Gaussian distribution defined by its mean and standard deviation. If the critical contact forces for tensile and shear failure of a bond (S_n and S_t) are normalized by the nominal area $2Rt$, then the tensile and shear bond strengths can be expressed in stress units as $\sigma_{cr} = S_n/(2Rt)$ and $\tau_{cr} = S_t/(2Rt)$, respectively. *Hazzard et al.* [2000] observed that while the mean value of the bond strength controls the brittle strength of a bonded assemblage, the standard deviation influences the stability of the post-peak behavior (with a more gentle post-peak slope corresponding to a larger standard deviation). *Boutt and McPherson* [2002] also observed that a higher ratio of shear to normal bond strength seems to promote shear localization along a well-defined planar structure. *Hazzard et al.* [2000] used bond strengths with ratios of $\tau_{cr}/\sigma_{cr} = 1.5$ for two granites and $\tau_{cr}/\sigma_{cr} = 1.0$ for the more ductile chalk. Since we focus on ductile failure and compaction localization in this study we set $\tau_{cr} = \sigma_{cr}$ with a mean value of 100 MPa and standard deviation of 25 MPa (Table 1). For comparison, *Hazzard et al.* [2000] chose a mean value of 100 MPa and standard deviation of 30 MPa for Ekofisk chalk, but significantly higher values for two granites. As elaborated later section these choices of bond strengths result in simulated yield stresses that are in reasonable agreement with a sandstone of comparable porosity and grain size.

[17] Unlike most previous models, we incorporated here a third damage mechanism involving intragranular failure characterized by the tensile strength σ_{cr}^g , which is expected to be appreciably higher than the intergranular tensile strength σ_{cr} . Previous studies have used values ranging from 0.1 to 0.75 for the ratio $\sigma_{cr}/\sigma_{cr}^g$ [*Bruno and Nelson*, 1991; *Boutt and McPherson*, 2002]. Such a range is plausible in light of fracture mechanics measurements on bicrystals and polycrystalline ceramics which show that the ratio between grain boundary fracture toughness and lattice fracture toughness falls in a similar range [*Class and Machlin*, 1966; *Krell et al.*, 1985; *Lawn*, 1993]. Here we will mostly show simulations with $\sigma_{cr}^g = 2\sigma_{cr} = 200$ MPa, but selected simulations with different values of σ_{cr}^g assigned to grains of different mineralogy will also be discussed.

[18] As noted earlier, we typically used a value of $\varepsilon = 0.01$ for the shrinkage parameter. Each episode of shrinkage would result in a reduction of the grain area by a factor of

0.02, and the movement of the neighboring grains toward the damaged grain could reduce the local porosity by as much as 0.02. If a particular grain undergoes N_{\max} numbers of shrinkage, then the local porosity could be reduced by as much as 8%, about half of the initial porosity in the assembly which is similar to microstructural observations in sandstones [*Menéndez et al.*, 1996; *Baud et al.*, 2004]. As indicated in Table 1, most of the micromechanical parameters are assumed to be constant here, except for selected simulations in which we lowered the strength parameters of a certain percentage of the bonds. Even though we have conducted parametric studies over a range of values, these simulations will not be presented since they are peripheral to the primary focus here which is on the influence of grain size and its distribution on failure mode.

2.3. Particle Size Distribution and Strength Heterogeneity

[19] An objective of this study is to explore and simulate how grain sorting and pore space heterogeneity influence the failure mode associated with compaction localization and the brittle-ductile transition in porous sandstones. As detailed in Table 2 disk assemblies corresponding to seven different size distributions were investigated. The initial areal porosities of these assemblies were almost identical, falling within a very narrow range of 0.159–0.167. The R5r1 assembly represents the homogeneous end-member, with disk radii basically constant. In the other six assemblies the disk radii were assumed to be uniformly distributed between the maximum and minimum values (R_{\max} and R_{\min}) given in Table 2. Five assemblies (R5r1, R45r12, R4r15, R33r2 and R25r3) had almost identical mean radii of $\bar{R} \sim 0.5$ mm, and three assemblies (R15r3, R2r3 and R25r3) had an identical ratio of $R_{\max}/R_{\min} = 3$.

[20] To explore the influence of strength heterogeneity induced by, for example, mineralogical differences or cementation, we considered in selected simulations two different sets of strength parameters. Specifically we will present results in which 30% of the bonds were identified to be weaker, with values for strength (τ_{cr} , σ_{cr} and σ_{cr}^g) equal to 0.8 of the strength of the other 70% of bonds in the assembly.

3. Discrete Element Simulations of Inelastic Behavior and Failure Mode

[21] To assemble a sample for DE simulations, the particles (with radii prescribed according to one of the seven distributions) were randomly deposited inside a rectangular domain 40 mm wide and 90.3 mm long. Since the radius distributions and average radii used were quite different in the seven assemblies, the number of disks required to attain an areal porosity of $\sim 16\%$ varies among

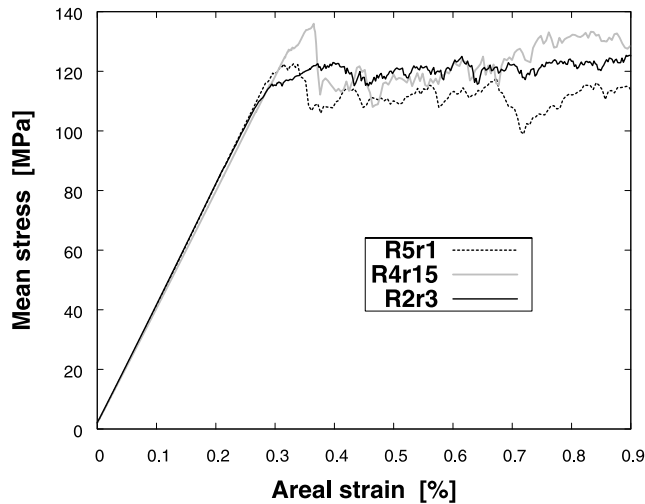


Figure 1. Confining pressure as a function of areal change of three assemblies.

the assemblies in the range of 3866 to 10741 (Table 2). The circular particles were allowed to overlap and after they had been generated, a relaxation algorithm in the PFC^{2D} code was implemented to minimize the contact force heterogeneity due to non-uniform overlap between particles. A relatively small stress of 1 MPa was then applied to the relaxed assembly in both the axial and lateral directions. This represents the reference state that will be compared with deformed states subjected to additional loading.

[22] With numerical servo-control we applied axial and lateral stresses along three different loading paths to simulate hydrostatic, conventional triaxial and uniaxial strain tests [Wang, 2003]. Only simulations from the first two paths will be discussed in this paper. To simulate a hydrostatic test in the laboratory, equal increments of axial and transverse stresses were simultaneously applied to the assembly. To simulate a conventional triaxial test equal amount of axial and lateral stresses were first applied, and then the axial stress was increased while keeping the lateral “confining” stress constant. Because the DE method is a dynamic formulation, a damping mechanism (corresponding to microscopic processes such as internal friction and wave scattering) is invoked to dissipate kinetic energy [Hazzard et al., 2000; Potyondy and Cundall, 2004]. To simulate quasi-static loading, it is necessary to use a relative high numerical damping factor (of 0.7 or larger) in the PFC^{2D} code. Our simulations were all conducted with a damping factor of 0.8.

[23] We will use the convention that compressive stresses and strains are positive. The mechanical quantities are all normalized assuming the third dimension has unit thickness. The principal stresses in the axial and transverse directions will be denoted by σ_1 and σ_2 , respectively and their mean value is given by $P = (\sigma_1 + \sigma_2)/2$. Their difference $Q = \sigma_1 - \sigma_2$ will be referred to as “differential stress”. The principal strains in the axial and transverse directions will be denoted by ε_1 and ε_2 , respectively and the areal strain is given by $\theta = \varepsilon_1 + \varepsilon_2$. In this model the stress-strain relation is linearly elastic until the local stress is sufficiently high to initiate bond breakage or intragranular failure, beyond which inelastic strain will accumulate in the form of relative grain

movement and shrinkage. For comparison with laboratory data on AE activity, we will refer to the proxy provided by a damage event (which may involve grain crushing or breakage of a bond by either tension or shear) in the DE simulation as an “AE event”. Similarly the statistics of such damage provide proxies for AE rate and AE counts as measured in the rock mechanics laboratory.

3.1. Critical Pressure for the Onset of Pore Collapse

[24] The mechanical response to equal biaxial loading is illustrated by our simulations for R5r1, R4r15, and R2r3 (Figure 1). Although the particle size distributions varied, the areal strain in each aggregate increased linearly with mean stress following an almost identical slope up to a critical mean stress $P^* \sim 120$ MPa. Significant inelastic strain then developed while the mean stress fluctuated by small stress drops about the critical stress level. The DE simulations are qualitatively similar to mechanical data on the onset and development of pore collapse in porous clastic and carbonate rocks induced by hydrostatic loading [Zhang et al., 1990; Vajdova et al., 2004b].

[25] For porous sandstones Zhang et al. [1990] developed a Hertzian fracture mechanics model which predicted that the critical pressure P^* for the onset of grain crushing and pore collapse would scale with porosity ϕ and grain radius R according to $P^* \propto (\phi R)^n$ with $n = -1.5$. As illustrated in Figure 2, critical pressure data of porous sandstones, soil and glass beads compiled by Wong et al. [1997] approximately follow this trend. The critical pressures for the seven assemblies from our DE simulations have values comparable to sandstones with similar porosity and grain size. Microstructural observations on these porous aggregates

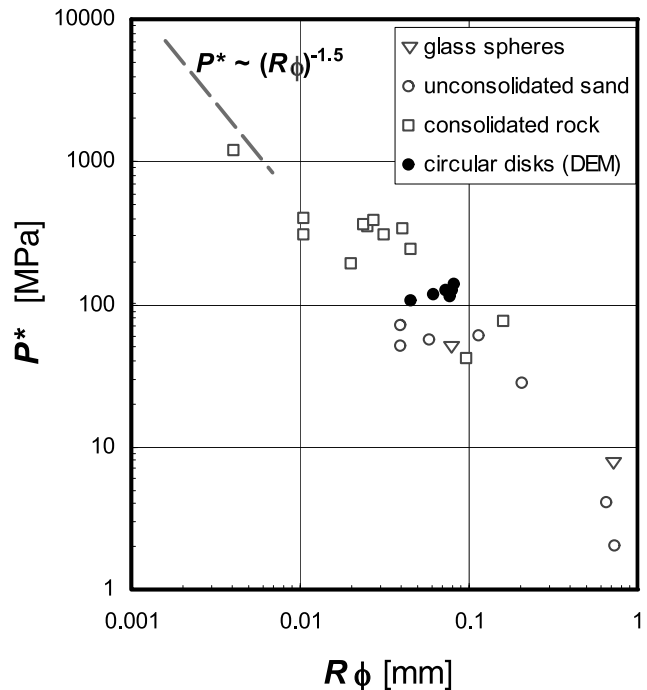


Figure 2. Critical pressure P^* for onset of pore collapse. DE simulation data from this study fall on the trend for laboratory data for clastic rocks, sand and glass spheres compiled by Wong et al. [1997].

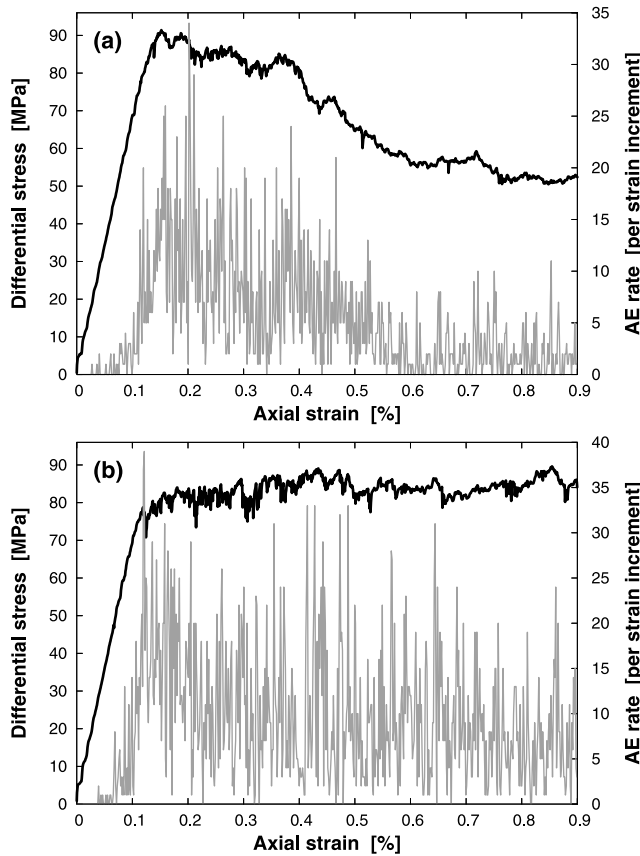


Figure 3. Differential stress (solid line) and AE rate (gray line) as functions of axial strain of R2r3 at lateral stresses of (a) 10 MPa, and (b) 40 MPa.

show that damage in the hydrostatically compacted samples developed as clusters of crushed grains and collapsed pores [Zhang *et al.*, 1990; Menéndez *et al.*, 1996]. Clusters of similar damage were observed in the simulated assemblies that had been stressed beyond the critical level.

3.2. Transition From Dilatant Failure to Shear-Enhanced Compaction

[26] To explore the effect of confinement on the transition of failure mode from brittle faulting to shear-enhanced compaction, we conducted simulations with the lateral stress σ_2 fixed at a value ranging from 8 MPa to 70 MPa. Figures 3 and 4 illustrate the inelastic and failure behavior in sample R2r3. The simulated behavior at a relatively low confinement of $\sigma_2 = 10$ MPa is shown in Figure 3a. Initially the differential stress increased linearly with axial strain. It ultimately attained a peak value, beyond which strain softening was observed. The AE rate started to increase at a differential stress of about half of the peak stress, and attained a maximum near the peak stress and then decayed gradually with further softening. At the higher confinement of $\sigma_2 = 40$ MPa (Figure 3b), the differential stress did not show an absolute maximum. After an initial linear response, the stress level continued to climb gradually but this overall trend of strain hardening was punctuated by small stress drops accompanied by episodic AE surges.

[27] Data for the mean stress as a function of areal strain in five simulations with σ_2 ranging from 8 MPa to 70 MPa

are presented in Figure 4. For reference the linear portion of the “hydrostats” for equal biaxial loading (from Figure 1) is also included. Fundamental differences in the inelastic yield behavior related to the brittle-ductile transition were observed, and accordingly the data can be categorized into two groups. While dilatancy was observed at lateral stresses of 8, 10 and 20 MPa, the inelastic behavior at higher lateral stresses of 30, 50, and 70 MPa was typical of shear-enhanced compaction.

[28] These simulations thus reproduce key attributes of AE activity and mechanical data associated with the transition from dilatant failure to shear-enhanced compaction in porous sandstones [Wong *et al.*, 1997]. Hence we can use the same methodology for analyzing laboratory data to identify the critical stresses C' (for the onset of dilatancy) and C^* (for the onset of shear-enhanced compaction) with the stress levels at which the deviatoric response deviates from the hydrostatic response in such curves. Our data for these critical stresses in the three porous aggregates R5r1, R4r15, and R2r3 are compiled in Figure 5 in the (Q, P) stress space. Both the absolute stresses and normalized stresses are shown. In agreement with laboratory data there is an overall trend for the compactive yield stress C^* to decrease with increasing mean stress, falling on a yield cap that is approximately elliptical [Wong *et al.*, 1997; Baud *et al.*, 2004].

3.3. Micromechanics of Shear Localization

[29] Since brittle faulting has been extensively investigated using the DE method [e.g., Bruno and Nelson, 1991; Hazzard *et al.*, 2000; Boutt and McPherson, 2002] we will focus our discussion here only on those micromechanical aspects related to grain crushing which were not incorporated into previous modeling efforts. With reference to the differential stress versus axial strain curve for R2r3 in Figure 6a, we separate the deformation into four sequential stages. Stage I corresponds to the initial linear deformation and onset of dilatancy. Stage II is in the vicinity of the peak stress, stage III corresponds to the development of strain softening, and

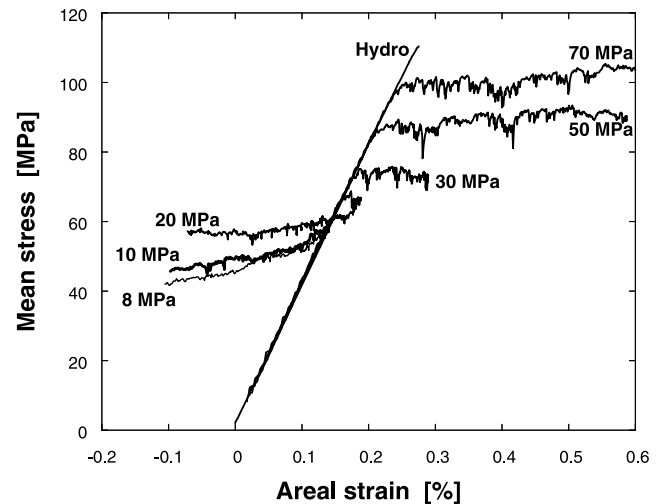


Figure 4. Mean stress as a function of areal strain in R2r3 under six lateral stresses ranging from 8 MPa to 70 MPa. For reference the data for equal biaxial stresses are also shown and labeled as Hydro.

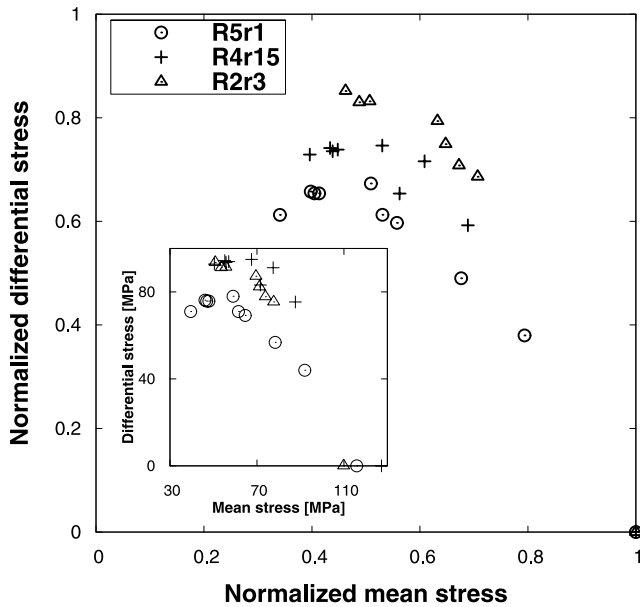


Figure 5. The compactive yield stress at the onset of shear-enhanced compaction are plotted in the differential stress Q -mean stress P space. Absolute magnitudes of stress are plotted in the inset figure, and normalized stresses (P/P^* , Q/P^*) are plotted in the main figure. Simulations from three different assemblies are included.

at stage IV the stress has approached the residual strength. The three different types of damage (extensile and shear bond breakages, and grain crushing) accumulated toward the end of stage IV are mapped out in Figure 6b. The spatial distributions of AE accumulated in stages I through IV are shown in Figures 6c–6e.

[30] The spatiotemporal distributions of AE activity we observed are qualitatively similar to previous DE simulations [e.g., Hazzard *et al.*, 2000; Boutt and McPherson, 2002; Li and Holt, 2002] as well as laboratory measurements [e.g., Lockner *et al.*, 1992]. Localization of AE activity was not evident until stage II near the peak stress. Our simulations show that the incorporation of grain crushing has minimal influence on these patterns in both stages I and II since the damage in these stages was dominated by extensile and shear bond breakages. However, it can be seen from Figure 6b that grain crushing was pervasive inside the shear band once strain had localized. That grain crushing represents an important micromechanical process during the development of shear deformation bands is in agreement with microstructural observations on porous sandstones [e.g., Menéndez *et al.*, 1996; Mair *et al.*, 2000; Wu *et al.*, 2000].

3.4. Micromechanics of Compaction Localization

[31] The micromechanics associated with the transition from brittle faulting to cataclastic flow was elucidated by the AE activity simulated in R2r3 at the lateral stresses of 8, 30, 50 and 70 MPa (Figure 7). In this porous aggregate with a relatively broad particle size distribution, the damage distribution became more diffuse and delocalized at higher confinements. Such spatiotemporal evolution of damage is akin to that mapped out by microstructural observations in failed samples of Darley Dale sandstones [Wu *et al.*, 2000].

[32] An important observation from our simulations is that whether damage would be localized or delocalized under high confinement hinges on the particle size distribution. Figure 8 shows the spatial distribution of AE activity at the same lateral stress of 70 MPa in six aggregates. The grain sorting is inversely related to the ratio R_{\max}/R_{\min} , which has values of 1.0, 1.2, 1.5, 2.0, 3.0, and 3.0, respectively in Figures 8a–8f. In the perfectly sorted sample R5r1, made up of a monodisperse assembly of disks, the localization of compaction into discrete bands subperpendicular to σ_1 was clearly observed in our simulations. At a given strain interval (given by the color code) the AE activity would mostly be confined within a relatively narrow zone. The relative locations of such bands seem uncorrelated, in that AE activity in the subsequent strain interval might localize some distance from the current discrete band. The spatial evolution of damage in this simulation is similar to microstructural observations of the development of discrete compaction bands in the Bentheim and Diemelstadt sandstones [Wong *et al.*, 2001; Baud *et al.*, 2004] and recent AE measurement in the Bleurswiller sandstone [Fortin *et al.*, 2006], as well as field observations in Utah and Nevada [Hill, 1989; Mollema and Antonellini, 1996; Sternlof *et al.*, 2005].

[33] In the polydisperse samples R45r12 and R4r15 a compaction band would tend to first widen with increasing strain before jumping to another band at a different location (Figures 8b and 8c). The development of such diffuse compaction bands is akin to the AE and microstructural observations in Castlegate sandstone [Olsson, 1999; Olsson and Holcomb, 2000; DiGiovanni *et al.*, 2000]. In the poorly sorted samples (Figures 8d, 8e and 8f) the damage distributions are fairly delocalized, indicating that strain localization was inhibited.

[34] The relation between localization mode and temporal AE activity is illustrated in Figures 9 and 10. In Figure 9a we identified seven discrete compaction bands in the monodisperse sample R5r1, which can be matched to distinct episodes of stress drops and AE surges marked in Figure 9b. In contrast, episodic stress drops or AE surges cannot be readily identified in Figures 10a–10e for the other five samples, which failed by the development of diffuse bands and delocalized cataclastic flow. Such a qualitative difference in AE activity is similar to that observed by Baud *et al.* [2004] in laboratory measurements, who referred to the episodic behavior (Figure 9b) as “p-type” and those in Figure 10 as “m-type”.

[35] To investigate whether strength heterogeneity may inhibit the development of discrete compaction bands, we conducted simulations on a monodisperse aggregate (R5r1MC) with uniform disk radius, but unlike R5r1 30% of the bonds in this mixed assembly had strengths reduced by 0.2. The simulations for a lateral stress of 70 MPa are presented in Figure 11a. The compactive yield stress was significantly lower than that of the homogeneous assembly (Figure 9a). Notwithstanding the strength heterogeneity, this mixed assembly showed a relatively strong tendency to develop discrete compaction bands in a manner similar to that in the homogeneous assembly. We also conducted simulations on a mixed aggregate R4r15MC which had a radius distribution identical to that in R4r15. The results for a lateral stress of 70 MPa are shown in Figure 11b. Compaction

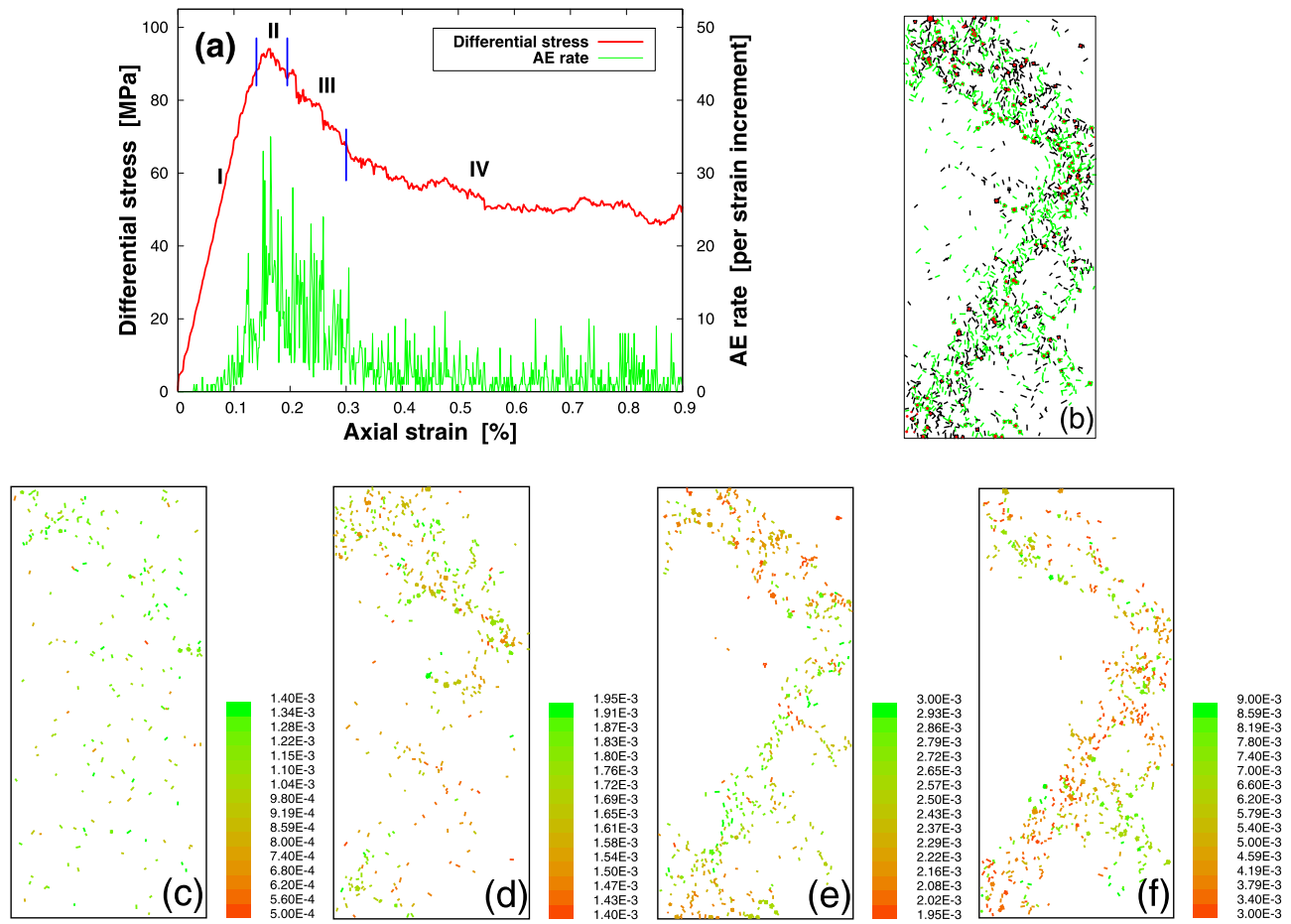


Figure 6. (a) Differential stress and AE rate as functions of axial strain in R2r3: four distinct stages of deformation can be identified as discussed in the text. (b) Damage accumulated at the end of stage IV: the tensile and shear bond breakages are shown in black and green, respectively. The crushed grains are shown as solid circles in red. The damage accumulated through stages (c) I, (d) II, (e) III and (f) IV are also shown. Color codes in these four figures are in units of axial strain.

localization for the mixed aggregate in this case seems to be more diffuse than the homogeneous aggregate.

4. Discussion

[36] In this study we have developed a technique whereby intragranular failure can be incorporated into a 2-dimensional DE model. The model captures many key mechanical attributes of the brittle-ductile transition in porous granular rocks, including brittle faulting at low confinement, shear-enhanced compaction at high confinement and an approximately elliptical cap for the onset of compactive yield. Furthermore, the spatiotemporal evolution of damage associated with the two failure modes mimic laboratory data on AE activity and microstructural observations in failed samples, thus providing useful insights into the micromechanics of shear localization and compaction localization in porous rocks.

[37] In our model pore collapse is simulated by shrinking the disk radius by a constant factor of ε on the order of 0.01. It should be noted that other approaches have been proposed for modeling such a micromechanical process. In his finite element model *Amitrano* [2003] simulated the damage

accumulation in an element by reducing its elastic moduli. We have conducted numerical experiments using this approach, which showed that compaction localization can develop only if a drastic reduction of moduli is assigned to a failed grain [*Wang*, 2003]. Indeed the most extreme scenario would be to assign zeros to the moduli, which represents complete removal of the failed grains from the assembly. This scenario corresponds to the approach taken by *Couroyer et al.* [2000] and *Markatos and Bolton* [2005] in their DE modeling of powder crushing and compaction band formation. Such an approach induces anomalously high stress drops associated with pore collapse.

[38] Another approach was undertaken by *Li and Holt* [2002] and *Boutt and McPherson* [2002], who modeled the rock as an assemblage of “superparticles” made up of clusters of bonded particles. Breakage of bonds inside a superparticle mimics grain crushing, and the relative movement of particles within the cluster contributes to pore collapse. *Li and Holt* [2002] demonstrated that their approach can simulate many of mechanical aspects of brittle-ductile transition in porous clastic rocks that our model also captures. However, the failure modes they reproduced in their simulations seem to be restricted to shear bands and diffuse compaction bands.

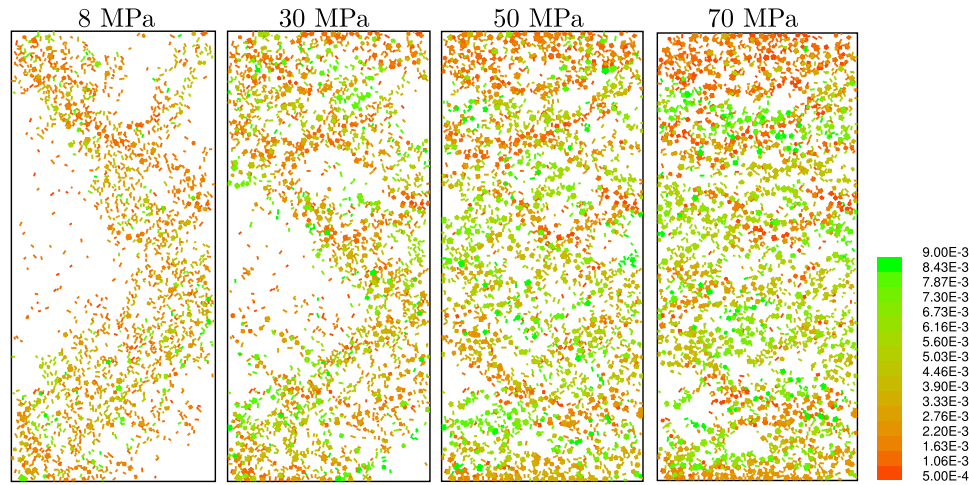


Figure 7. Spatial distribution of damage in R2r3 under lateral stresses of (a) 8 MPa, (b) 30 MPa, (c) 50 MPa and (d) 70 MPa. Color code is in units of axial strain.

That discrete compaction bands were not observed is possibly because they did not systematically vary the size distribution of the particles embedded inside the super-particles.

[39] Although these DE models are capable of reproducing many attributes of the stress-strain curves and failure modes, they are somewhat limited in their ability to capture the micromechanical complexity, especially in relation to grain crushing and pore collapse. Even if the grains can indeed be idealized as spherical particles or circular disks, grain crushing will naturally result in angular fragments of smaller sizes. Some fragments may also chip off and fall into the void space. How to realistically capture these complex processes involving significant changes in grain angularity, size distribution and coordination number remains a major challenge in DE modeling. In relation to our grain shrinkage model, although our simulations have demonstrated that it can reproduce many of the macroscopic attributes of porous sandstone deformation, we have yet to demonstrate the connection between grain shrinkage and the micromechanical processes inferred from microstructural observations [e.g., *Menéndez et al.*, 1996; *Baud et al.*, 2004].

[40] To what extent can our DE model simulate pore collapse as a key mechanism of inelastic compaction? To elucidate the connection between grain shrinkage and pore collapse in our model, we analyze the strain partitioning in our simulations by comparing the areal strain ε' due to grain shrinkage and the bulk areal strain ε . Since ε' represents the relative reduction in solid grain volume, the difference $\varepsilon - \varepsilon'$ corresponds to areal strain due to pore collapse, that derives from grain rearrangement triggered by grain shrinkage. In Figure 12 we present our data for three assemblies under a lateral stress of 70 MPa at several stages of deformation. In each of these simulations inelastic yield and grain shrinkage did not initiate until a bulk strain of $\varepsilon \approx 0.007$ was attained, beyond which a strain increment $\Delta\varepsilon'$ due to grain shrinkage would typically trigger an increment of bulk strain $\Delta\varepsilon \approx 2\Delta\varepsilon'$, and therefore $\Delta(\varepsilon - \varepsilon') \approx \Delta\varepsilon/2$ which implies that pore collapse accounts for about half of the bulk strain. A ratio of strain partitioning comparable to that shown in Figure 12 was observed in most of our simulations.

[41] While this demonstrates that pore collapse triggered by grain shrinkage is an important mechanism in our DE model, it should be emphasized that since bulk strain and porosity reduction measurements show that the latter probably accounts for most of the former, the strain partitioning in our model is such that it underestimates the contribution of pore collapse to the inelastic volumetric strain and overestimates the contribution from solid volume reduction. Although the grain volume would decrease if small grain fragments chip off and fall into the void space, it is likely this represents only a minor contribution to the overall volumetric strain. Why does our model require a disproportionately large shrinkage to fit the experimental data? This is possibly related to its limited capability to represent the significant changes in grain angularity, size distribution and coordination number that result from grain crushing. As a proxy mechanism to the cooperative effects of these very complex processes, relatively large grain shrinkage are required to induce spatial heterogeneity of damage as well as macroscopic stress and strain which are comparable to experimental observations. For a similar reason, unrealistically large reductions in elastic stiffnesses must be invoked in DE models that use such a mechanism to simulate grain crushing.

[42] Even though grain shrinkage in our model was assumed to be locally isotropic, the spatial distribution of damage and macroscopic strain induced by nonhydrostatic loading were anisotropic. Since microstructural data [*Menéndez et al.*, 1996; *Baud et al.*, 2004] indicate that microcracking related to grain crushing can be moderately anisotropic, one may argue that the local damage should also be modeled as anisotropic. However, in the absence of microstructural data that can better constrain the anisotropy (especially regarding pore collapse), incorporating this additional complexity seems unwarranted at this stage of model development.

4.1. Local Stress Perturbation Induced by Porosity Reduction

[43] Our observation that discrete compaction bands can readily develop in a relatively homogeneous assembly is in basic agreement with the 2-dimensional network modeling

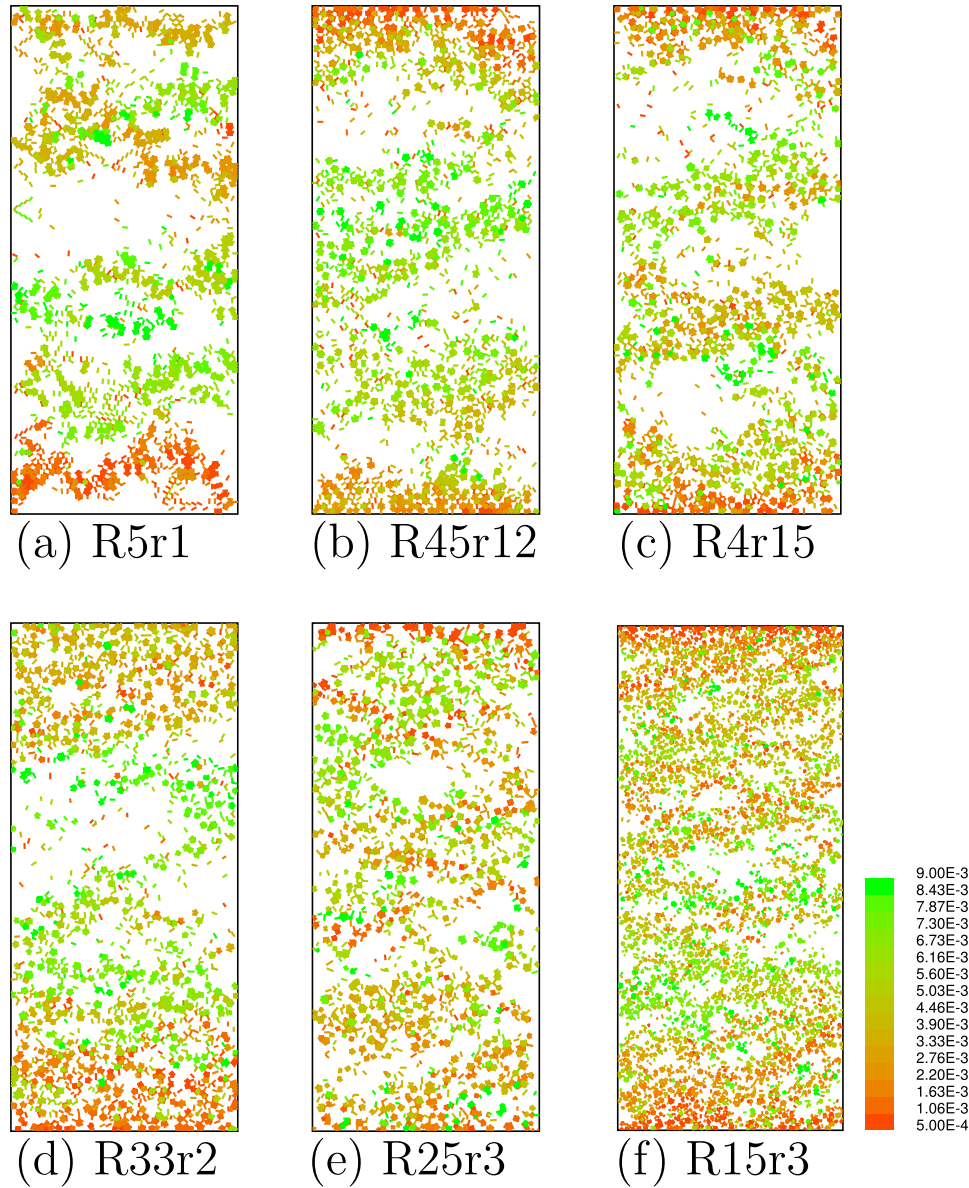


Figure 8. Spatial distribution of damage in (a) R5r1, (b) R45r12, (c) R4r15, (d) R33r2, (e) R25r3 and (f) R15r3 under lateral stress of 70 MPa. Note that the mode of compaction localization was more diffuse for a more heterogeneous assembly. Color codes in these figures are in units of axial strain.

results of *Katsman et al.* [2005]. Since the network topology was fixed to be triangular, they could introduce heterogeneity or “disorder” into the system by changing the statistical distribution of bond strength. Using a Gaussian strength distribution *Katsman et al.* [2005] observed that the development of failure by distributed cataclastic flow, diffuse compaction bands and discrete compaction bands in network assembly with large, small and no disorder, respectively.

[44] In the model of *Katsman et al.* [2005] porosity reduction was simulated by shortening the bond length by a constant ratio, which is analogous to our grain shrinkage mechanism. To analyze the local stress perturbation induced by porosity reduction *Katsman and Aharonov* [2006] and *Katsman et al.* [2006] introduced the concept of “transformational strain” as defined in the classic work of *Eshelby*

[1957]. An analogous approach was considered by *Sternlof et al.* [2005]. Here we follow their approach, adopting this conceptual model to analyze the local stress perturbation and its influence on the propagation of discrete compaction band in our DE model. We will consider a square Eshelby inclusion with length $2L$. Two types of observations motivated this choice of a square inclusion in our conceptual model. The first is related to the average coordination number, which in our simulations is ~ 4 . This value is typical of 2-dimensional systems of circular disks, which have coordination numbers significantly lower than those of 3-dimensional systems made up of spheres [*Makse et al.*, 2000]. The second is related to the configuration of “force chains” we observed in the perfectly sorted system R5r1 (Figure 13). Previous DE simulations have demonstrated that, as a rule, the applied load is not distributed homoge-

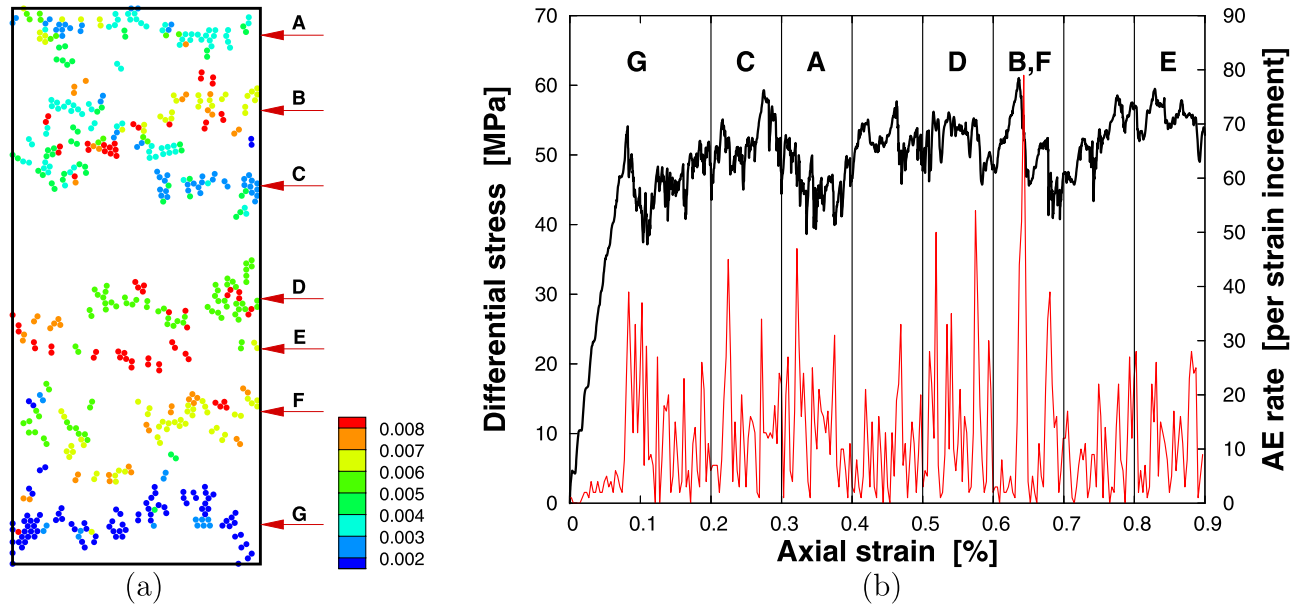


Figure 9. Sequential development of discrete compaction bands in the perfectly sorted assembly R5r1. At least seven bands can be identified as distinct tabular clusters in (a) the spatial distribution of damage, which can be identified with stress drops and AE surges in (b) the differential stress (black line) and AE rate (red line) as functions of axial strain. Color codes in the figure are in units of axial strain.

neously among the multiplicity of bonds in the assembly [e.g., Liu *et al.*, 1995; Radjai *et al.*, 1996; Makse *et al.*, 2000]. If the maximum principal stress is σ_1 , then the externally applied load would be supported by a small subset of bonds which are located along localized force chains aligned subparallel to σ_1 . A number of such axial chains can be identified in the snapshot at time $t = 0^-$ (Figure 13a). With the nucleation and propagation of pore collapse (Figures 13b–13f), a disproportionate amount of the applied load was instantaneously transferred to a narrow network of force chains embedded inside the discrete compaction band. The chains connect to form polygons with sides approximately equal in length. Many of these unit cells seem to be squares, but a number of pentagons and hexagons may also be recognized.

[45] To analyze the local stress induced in such a regular geometric configuration, we will consider a square inclusion with the two diagonals aligned with σ_1 and σ_2 , respectively (Figure 14a). The inelastic volumetric strain in the vicinity of a square network of force chains was approximated by the application of an isotropic transformational strain [Eshelby, 1957] to the square inclusion. In the context of our grain shrinkage mechanism, if the transformational strain is denoted by $\varepsilon_1^T = \varepsilon_2^T = \varepsilon^T$, then we expect $\varepsilon^T \approx \varepsilon$, the shrinkage parameter in our DE model.

[46] The transformational strain considered here is identical to that due to thermal mismatch in an inclusion (with a lower thermal expansivity) embedded in a thermoelastic matrix [Evans, 1978]. The equivalent thermoelastic problem for a square inclusion was analyzed by Fredrich and Wong [1986], and the pertinent mathematical results are summarized in Appendix A. The stress perturbations at the four corners of the inclusion (with length $2L$) are illustrated in Figure 14a. At the two corners B and D, the stress perturbation due to the transformational strain ε^T is given by a tensor with the axial and transverse principal compo-

nents given by $\Delta\sigma_1 = \Delta\sigma$ and $\Delta\sigma_2 = -\Delta\sigma$, which, for $y = 0$, can be expressed as

$$\Delta\sigma(x) = \frac{E\varepsilon^T}{2\pi(1-\nu)} \ln \left[\frac{(x + \sqrt{2}L)^2 + 2L^2}{x(x + 2\sqrt{2}L)} \right] \quad (1)$$

where E and ν denotes the Young's modulus and Poisson's ratio, respectively.

[47] The stress for $y = 0$ has a logarithmic singularity at a corner, but decays with distance away from the corner. Hence the stress when averaged over a distance ℓ is bounded and given by

$$\begin{aligned} \overline{\Delta\sigma}(\ell) &= \frac{\int_0^\ell \Delta\sigma(x) dx}{\ell} \\ &= \frac{E\varepsilon^T}{2\pi(1-\nu)} \left\{ \frac{2\sqrt{2}}{\rho} \left[\tan^{-1} \left(\frac{\rho + \sqrt{2}}{\sqrt{2}} \right) - \frac{\pi}{4} \right] \right. \\ &\quad \left. + \frac{\sqrt{2}}{\rho} \ln \left[\frac{2((\rho + \sqrt{2})^2 + 2)}{\rho + 2\sqrt{2}} \right] + \ln \left[\frac{(\rho + \sqrt{2})^2 + 2}{\rho(\rho + 2\sqrt{2})} \right] \right\} \end{aligned} \quad (2)$$

with $\rho = \ell/L$. The average stress perturbation $\overline{\Delta\sigma}$ decreases with increasing distance ℓ over which the averaging was performed, and in particular $\overline{\Delta\sigma}(L) = 1.53 E\varepsilon^T/[2\pi(1-\nu)]$ and $\overline{\Delta\sigma}(2L) = 1.01 E\varepsilon^T/[2\pi(1-\nu)]$, which would have magnitudes of 244 MPa and 159 MPa, respectively assuming $E = 80$ GPa, $\nu = 0.2$ and $\varepsilon^T = \varepsilon = 0.01$. Such stress perturbations are comparable to the critical compressive stress for grain crushing $\sigma_{cr}^g = 200$ MPa we used in the DE simulations.

[48] When superposed on the “background” stress field such as that for $t = 0^-$ shown in Figure 14a, this significant enhancement of compressive stress in the axial direction

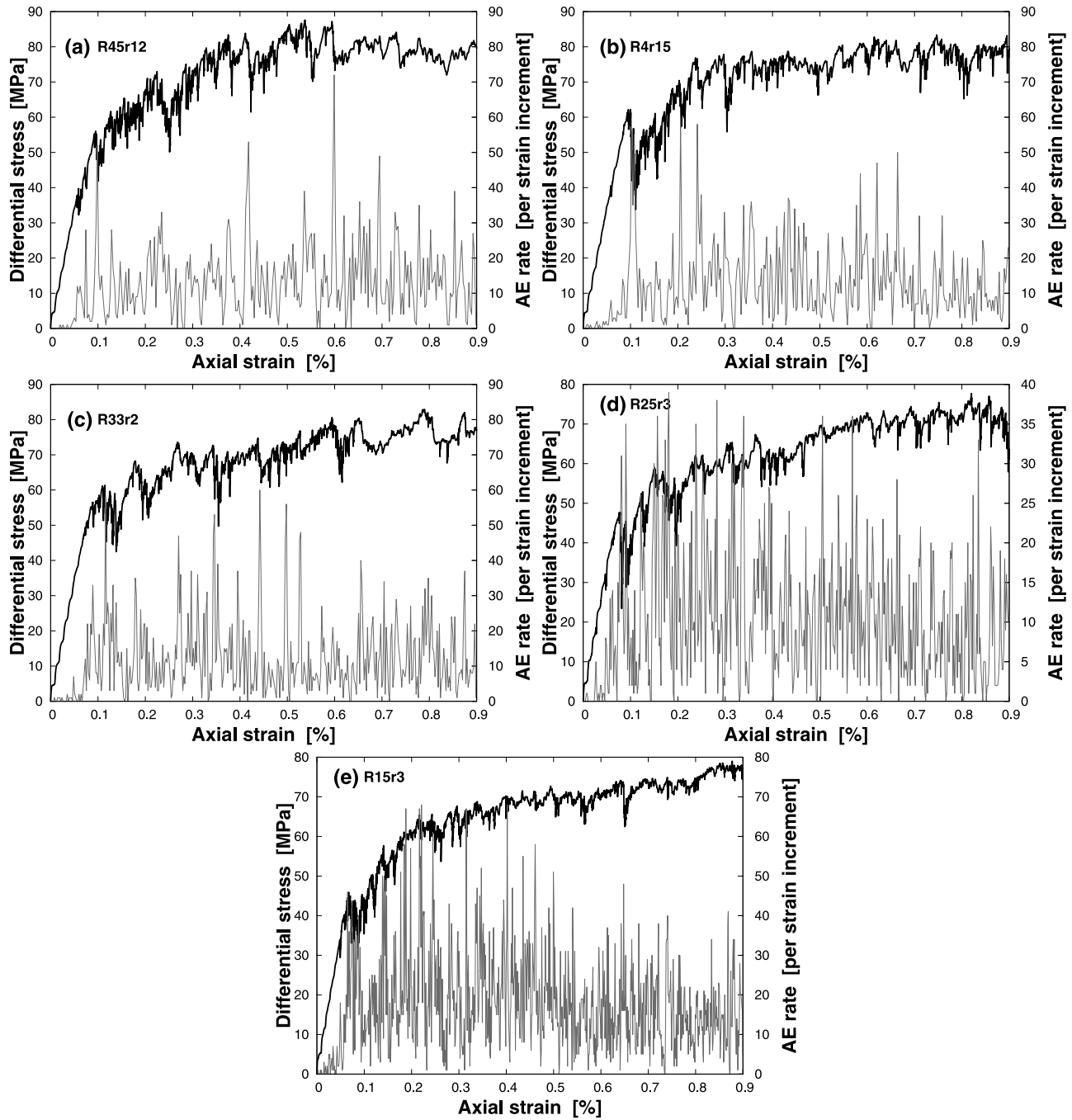


Figure 10. Differential stress (black line) and AE rate (gray line) in (a) R45r12, (b) R4r15, (c) R33r2, (d) R25r3 and (e) R15r3 at lateral stress of 70 MPa.

would promote grain crushing and pore collapse in the vicinity of the two corners B and D, thus promoting the lateral propagation of a compaction band along the σ_2 direction. In contrast, the stress perturbation at the corners A and C is given by a tensor with axial and transverse components given by $-\Delta\sigma$ and $\Delta\sigma$, respectively (Figure 14a). The very large tensile stress perturbation in the axial direction would significantly reduce the “background” compressive stress in the vicinity of the corners A and C, which would shield the grains above and below from grain crushing and accordingly confine the propagation of com-

paction localization along the σ_2 direction within a relatively narrow band.

[49] The square inclusion analyzed here probably represents an extreme scenario for the local stress perturbation, but it underscores the strong influence that the symmetry and geometric regularity have over the development of discrete compaction bands. One would expect lower stress concentrations if the diagonals of the square inclusion are not aligned perfectly along the σ_1 and σ_2 directions or if the sides of the polygons are not exactly equal, which are

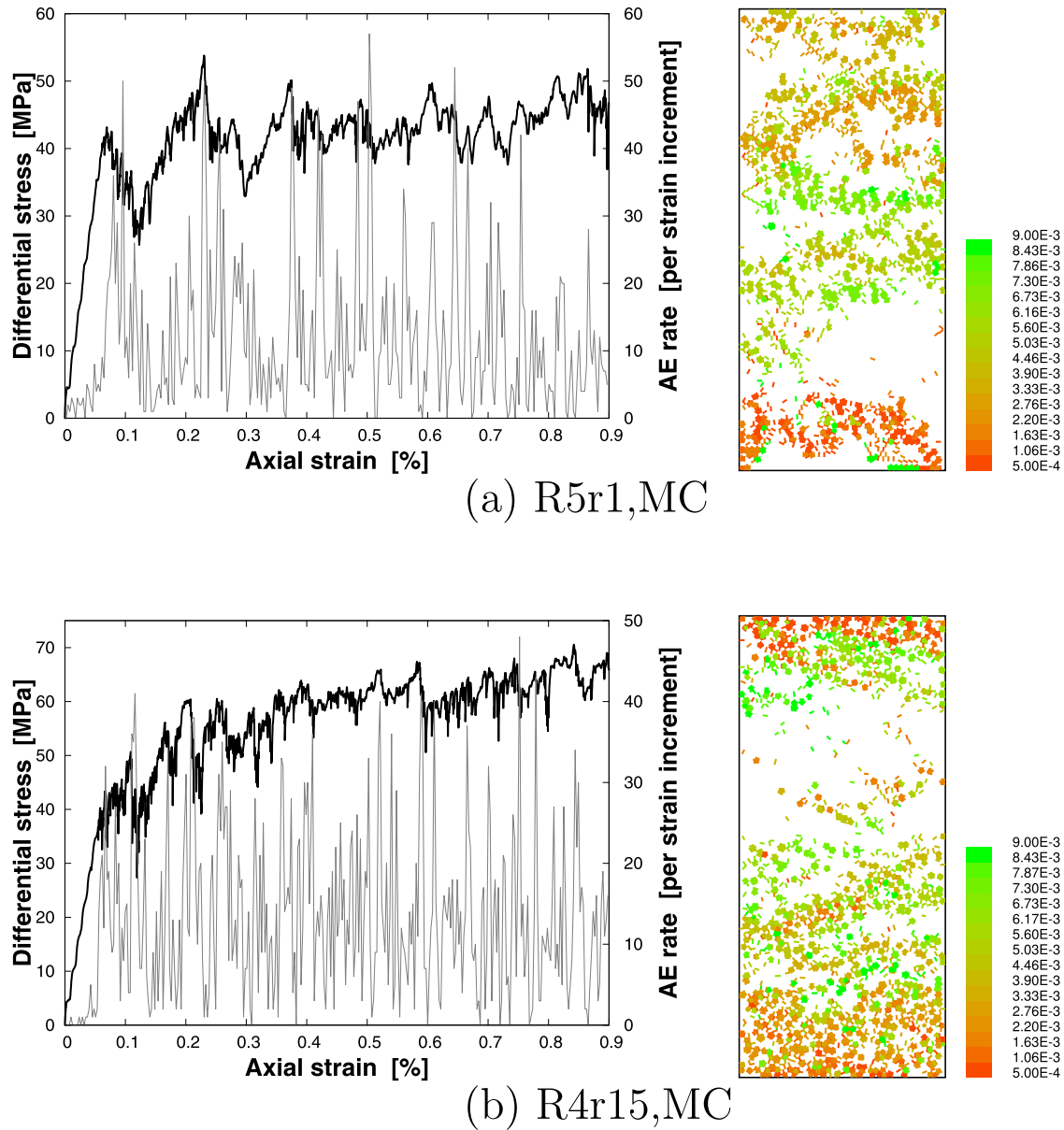


Figure 11. Differential stress (black line) and AE rate (gray line) as functions of axial strain (left), and spatial distribution of damage (right) in the mixed assemblies R5r1MC (a) and R4r15MC (b) at lateral stress of 70 MPa. Color codes in figures are in units of axial strain.

probably more common in assemblies with broader particle size distributions.

4.2. Discrete Versus Diffuse Compaction Bands: Effects of Grain Scale Heterogeneity

[50] The DE modeling presented here agrees with the network modeling of *Katsman et al.* [2005, 2006] which demonstrate that the development of discrete compaction bands is promoted in a relatively homogeneous granular aggregate, while diffuse band growth and distributed cataclastic flow are preferred modes of compaction in a more heterogeneous or disordered system. These results agree with the suggestion of *Klein et al.* [2001] that discrete compaction band is predominant in the Bentheim sandstone possibly because of its relatively homogeneous mineralogy (with 95% quartz, 3% orthoclase and 3% kaolinite) and

well-sorted grains. Some of the most systematic laboratory observations of discrete compaction bands have been in Bentheim sandstone [*Klein et al.*, 2001; *Wong et al.*, 2001; *Baud et al.*, 2004; *Vajdova et al.*, 2004a], and while the microstructure is akin to compaction bands observed in the field *Sternlof et al.* [2005] recently questioned to what extent laboratory tests represent a realistic proxy of the field structures since the stress levels to attain compactive failure in Bentheim sandstone are significantly higher than what is expected in the sandstone formations in the Kalibab monocline or Valley of Fire.

[51] Since then the development of discrete compaction bands has also been documented in the Diemelstadt [*Baud et al.*, 2004; *Louis et al.*, 2006] and Bleurswiller [*Fortin et al.*, 2006] sandstones, at significantly lower stress levels

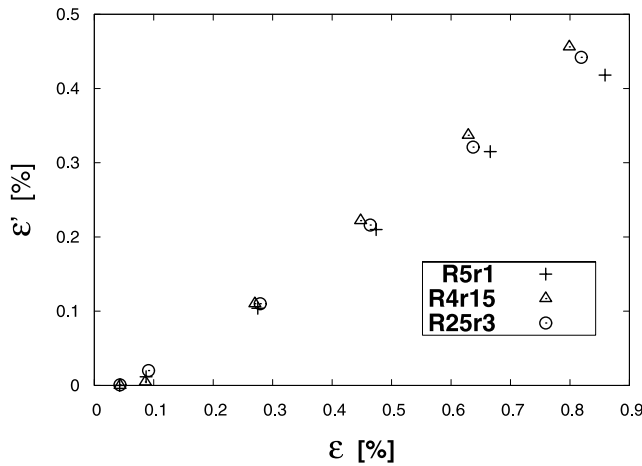


Figure 12. The areal strain ϵ' due to grain shrinkage versus bulk areal strain ϵ of three samples under lateral stress of 70 MPa.

$\sim 1/2$ and $1/4$, respectively of those in Bentheim sandstone. While they all have comparable porosity and average grain size, unlike the Bentheim sandstone the Diemelstadt sandstone has 26% feldspars and Bleurswiller sandstone has 30% feldspars and 20% of oxide-micas. It is plausible that these other minerals are weaker than quartz (due to, for example, more intense pre-existing damage), and accordingly strength heterogeneity would exist in these two sandstones similar to simulations with the mixed assemblies in

Figure 11, with compaction localization developing under appreciably lower failure stress.

[52] Given the variation in modal compositions among these three sandstones, what are the common grain-scale attributes that result in a relatively homogeneous structure favorable for the development of discrete compaction bands? A preliminary answer to this question was recently provided by *Louis et al.* [2007], who used X-ray computed tomography (CT) to map out pore space heterogeneity in several sandstones, including the Bentheim and Diemelstadt sandstones. Their analysis of CT data from high-resolution “industrial” CT (with resolution on the order of 0.1 mm) and synchrotron microtomography (with resolution down to several microns) show that the coefficient of variation (standard deviation normalized by the mean) of the CT-number may provide a useful measure of pore scale heterogeneity in these sandstones. In particular the Bentheim and Diemelstadt sandstones have coefficients of variation significantly lower than Berea and Rothbach sandstones which tend to develop compaction and shear bands in a diffuse manner [*Baud et al.*, 2004].

[53] Such CT measurements can also detail the 3-dimensional geometric complexities associated with the development of compaction localization. For discrete compaction bands that had developed in Diemelstadt sandstone, *Louis et al.* [2006] were able to characterize the width and tortuosity of these bands and their statistics. A limitation of the present study is our use of a 2-dimensional DE model, but such data from 3-dimensional CT imaging can now provide important

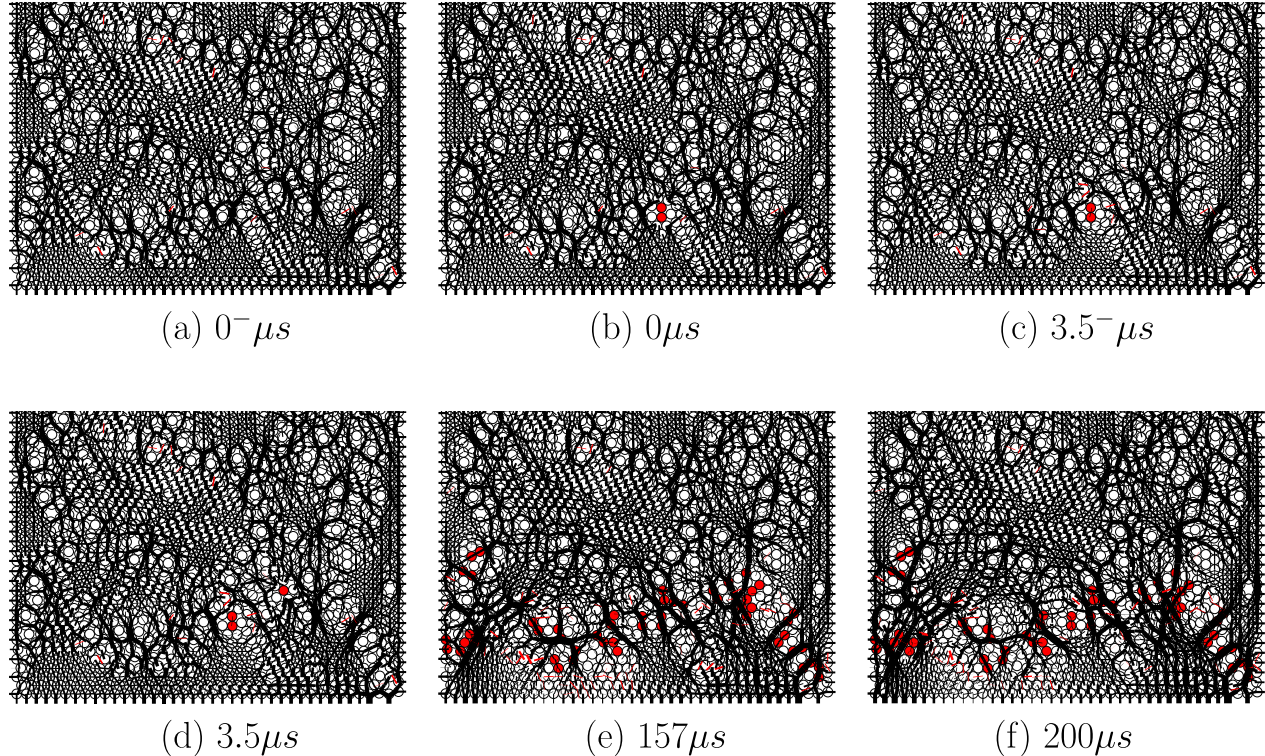


Figure 13. Evolution of force chains during the nucleation and propagation of a discrete compaction band in R5r1. Hollow and red solid circles mark the intact and crushed grains, respectively. The force chains are shown as short line segments, with thickness proportional to the force magnitude. The black and red chains correspond to compressional and tensile forces, respectively. The time steps correspond to iterations to attain quasi-static equilibrium in the DE assembly.

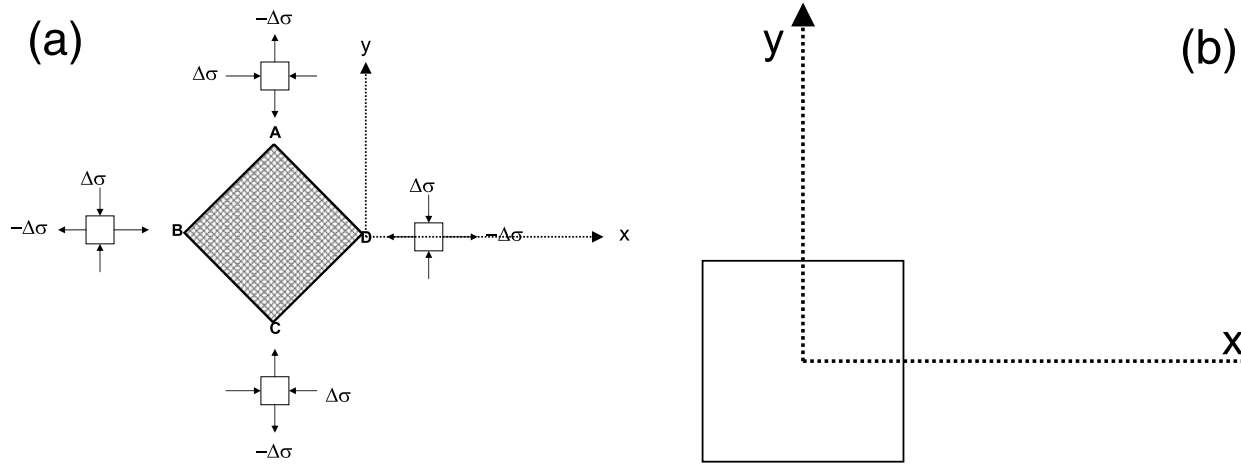


Figure 14. (a) Principal stress perturbations in the vicinity of the four corners of a square inclusion after it has been subjected to a compactive transformational strain. (b) Coordinate system used for the stress analysis for an Eshelby inclusion discussed in Appendix A.

constraints on 3-dimensional DE simulations, which should be the next step in our efforts to explore the intriguing phenomenon of compaction localization.

5. Conclusion

[54] Incorporating a grain shrinkage mechanism to simulate grain crushing and pore collapse, our model is capable of capturing key attributes of failure mode and damage evolution associated with the brittle-ductile transition in porous sandstones. With increasing confinement the failure mode changes from shear localization to distributed cataclastic flow. In the transitional regime, failure may occur by development of discrete compaction bands, diffuse compaction bands or high-angle shear bands.

[55] Our simulations show that the mode of compaction localization in the transitional regime is sensitively dependent on the grain size distribution. While the development of discrete compaction bands is promoted in a relatively homogeneous granular aggregate, diffuse band growth and distributed cataclastic flow are preferred modes of compaction in a more heterogeneous system.

[56] To explore why the development of discrete and narrow compaction bands seem to be promoted in a relatively homogeneous assembly, an Eshelby inclusion model was developed to derive an analytic approximation for the local stress perturbations in the vicinity of a crushed grain or pore collapse. This model shows that a transformation strain on the order of 0.01 can induce a local stress perturbation on the order of 100 MPa, thus promoting the lateral propagation of pore collapse.

Appendix A

[57] We summarize here the pertinent results for the 2-dimensional stress field outside a square inclusion subjected to a transformational strain as formulated by *Eshelby* [1957]. In the most general case, if the inclusion is subjected to a transformational strain ε_{ij}^T and the outward normal to its boundary is denoted by n_j , then the stress field in the matrix outside the inclusion is simply given by that induced by a layer of body force $C_{ijkl} \varepsilon_{kl}^T n_j$ acting over the inclusion

boundary, where C_{ijkl} denotes the elastic moduli. In an infinite, elastic space which is isotropic and homogeneous, the stress field due to a point force is given by Kelvin's solution; hence the stress field in the matrix can formally be obtained by performing a surface integration of all the contributions from the layer of body force acting over the inclusion boundary.

[58] In the 2-dimensional case one can derive the appropriate Green's function and perform an integration, using an approach similar to that of *Evans* [1978]. Specific to a square inclusion, one may also utilize the 3-dimensional stress solution for a cuboidal inclusion derived by *Chiu* [1977] to arrive at the square inclusion solution by taking the approach limits. Such an approach was taken by *Fredrich and Wong* [1986], and we summarize here their results relevant to the inclusion model in this study. With reference to the coordinate system shown in Figure 14b, if the square inclusion (of length $2L$) is subject to a compactive transformational strain $\varepsilon_{ij}^T = \varepsilon^T \delta_{ij}$, then the three independent components of the stress tensor in the matrix outside the inclusion are given by

$$\begin{aligned} \sigma_{xx} &= -\sigma_{yy} \\ &= \frac{E\varepsilon^T}{2\pi(1-\nu)} \left\{ \tan^{-1} \left[\frac{y+L}{x+L} \right] + \tan^{-1} \left[\frac{y-L}{x-L} \right] \right. \\ &\quad \left. - \tan^{-1} \left[\frac{y-L}{x+L} \right] - \tan^{-1} \left[\frac{y+L}{x-L} \right] \right\} \end{aligned} \quad (A1)$$

$$\begin{aligned} \sigma_{xy} &= \frac{E\varepsilon^T}{4\pi(1-\nu)} \\ &\times \ln \left\{ \frac{[(x+L)^2 + (y+L)^2]}{[(x+L)^2 + (y-L)^2]} \frac{[(x-L)^2 + (y-L)^2]}{[(x-L)^2 + (y+L)^2]} \right\} \end{aligned} \quad (A2)$$

[59] We have here corrected a typographic error in equation (A2) as given by *Fredrich and Wong* [1986]. The principal stresses shown in Figure 14a can then be

obtained from the above expressions after tensor transformation, as given by equation (1) in the text.

[60] **Acknowledgments.** We have benefited from discussions with Patrick Baud, Joanne Fredrich, John Rudnicki, Sheryl Tembe and Veronika Vajdova. We are grateful to Wei Zhu who checked the square inclusion calculation. The associate editor Ernie Rutter as well as reviewers Einat Aharonov and Emma Finch provided critical reviews. The research at the CEA Institute of Geophysics was supported by National Natural Science Foundation of China (NNSFC) under grant 40404008. The research at Stony Brook was partially supported by the Office of Basic Energy Sciences, U.S. Department of Energy under grant DE-FG02-99ER14996.

References

- Aharonov, E., and D. W. Sparks (2002), Shear profiles in granular layers, *Phys. Rev. E*, **65**(5), 051302.
- Amitrano, D. (2003), Brittle-ductile transition and associated seismicity: Experimental and numerical studies and relationship with the b value, *J. Geophys. Res.*, **108**(B1), 2044, doi:10.1029/2001JB000680.
- Antonellini, M. A., and D. D. Pollard (1995), Distinct element modeling of deformation bands in sandstone, *J. Struct. Geol.*, **17**, 1165–1182.
- Aydin, A. (1978), Small faults formed as deformation bands in sandstones, *Pure Appl. Geophys.*, **116**, 913–930.
- Aydin, A., R. I. Borja, and P. Eichhubl (2006), Geological and mathematical framework for failure modes in granular rock, *J. Struct. Geol.*, **28**, 83–98.
- Baud, P., E. Klein, and T. f. Wong (2004), Compaction localization in porous sandstones: Spatial evolution of damage and acoustic emission activity, *J. Struct. Geol.*, **26**, 603–624.
- Boutt, D. F., and B. J. O. L. McPherson (2002), Simulation of sedimentary rock deformation: Lab-scale model calibration and parameterization, *Geophys. Res. Lett.*, **29**(4), 1054, doi:10.1029/2001GL013987.
- Bruno, M. S., and R. B. Nelson (1991), Microstructural analysis of the inelastic behavior of sedimentary rock, *Mech. Mater.*, **12**, 95–118.
- Chiu, Y. P. (1977), On the stress field due to initial strains in cuboid surrounded by an infinite elastic space, *J. Appl. Mech.*, **44**, 587–590.
- Class, W. H., and E. S. Machlin (1966), Crack propagation method for measuring grain boundary energies in brittle materials, *J. Am. Ceram. Soc.*, **49**, 306–309.
- Couroyer, C., Z. Ning, and M. Ghadiri (2000), Distinct element analysis of bulk crushing: Effect of particle properties and loading rate, *Power Technol.*, **109**, 241–254.
- Cundall, P. A., and O. D. L. Strack (1979), A discrete numerical model for granular assemblies, *Geotechnique*, **29**, 47–65.
- Digby, P. J. (1981), The effective elastic moduli of porous granular rock, *J. Appl. Mech.*, **48**, 803–808.
- DiGiovanni, A. A., J. T. Fredrich, D. J. Holcomb, and W. A. Olsson (2000), Micromechanics of compaction in an analogue reservoir sandstone, *Proc. 4th North Am. Rock Mech. Symp.*, 1153–1160.
- Eshelby, J. D. (1957), The determination of the elastic field of an ellipsoidal inclusion and related problems, *Proc. R. Soc. Ser.*, **A241**, 376–396.
- Evans, A. G. (1978), Microfracture from thermal expansion anisotropy. I, Single phase systems, *Acta Metal.*, **26**, 1845–1853.
- Fortin, J., S. Stanchits, G. Dresen, and Y. Guéguen (2006), Acoustic emission and velocities associated with the formation of compaction bands in sandstone, *J. Geophys. Res.*, **111**, B10203, doi:10.1029/2005JB003854.
- Fredrich, J. T., and T.-f. Wong (1986), Micromechanics of thermally induced cracking in three crustal rocks, *J. Geophys. Res.*, **91**, 12,743–12,764.
- Hazzard, J. F., and K. Mair (2003), The importance of the third dimension in granular shear, *Geophys. Res. Lett.*, **30**(13), 1708, doi:10.1029/2003GL017534.
- Hazzard, J. F., and R. P. Young (2002), Moment tensors and micromechanical models, *Tectonophysics*, **356**, 181–197.
- Hazzard, J. F., and R. P. Young (2004), Numerical investigation of induced cracking and seismic velocity changes in brittle rock, *Geophys. Res. Lett.*, **31**, L01604, doi:10.1029/2003GL019190.
- Hazzard, J. F., R. P. Young, and S. C. Maxwell (2000), Micromechanical modeling of cracking and failure in brittle rocks, *J. Geophys. Res.*, **105**, 16,683–16,697.
- Hill, R. E. (1989), Analysis of deformation bands in the Valley of Fire State Park, Nevada, M. S. thesis, University of Nevada, Las Vegas.
- Holcomb, D. J., and W. A. Olsson (2003), Compaction localization and fluid flow, *J. Geophys. Res.*, **108**(B6), 2290, doi:10.1029/2001JB000813.
- Issen, K. A. (2002), The influence of constitutive models on localization conditions for porous rock, *Eng. Fract. Mech.*, **69**, 1891–1906.
- Issen, K. A., and J. W. Rudnicki (2000), Conditions for compaction bands in porous rock, *J. Geophys. Res.*, **105**, 21,529–21,536.
- Jaeger, J. C., and N. G. W. Cook (1979), *Fundamentals of Rock Mechanics*, 3rd ed., 593 pp., Chapman and Hall.
- Katsman, R., and E. Aharonov (2006), A study of compaction bands originating from cracks, notches, and compacted defects, *J. Struct. Geol.*, **28**(3), 508–518.
- Katsman, R., E. Aharonov, and H. Scher (2005), Numerical simulation of compaction bands in high-porosity sedimentary rock, *Mech. Mater.*, **37**, 143–162.
- Katsman, R., E. Aharonov, and H. Scher (2006), Localized compaction in rocks: Eshelby's inclusion and the spring network model, *Geophys. Res. Lett.*, **33**, L10311, doi:10.1029/2005GL025628.
- Klein, E., P. Baud, T. Reuschle, and T.-f. Wong (2001), Mechanical behaviour and failure mode of Bentheim sandstone under triaxial compression, *Phys. Chem. Earth Part A*, **26**, 21–25.
- Krell, A., J. Woltersdorf, E. Pippel, and D. Schulze (1985), On grain boundary strength in sintered Al_2O_3 , *Philos. Mag. Ser. A*, **51**, 765–776.
- Lawn, B. (1993), *Fracture of Brittle Solids. Second Edition*, 378 pp., Cambridge University Press, Cambridge.
- Li, L., and R. M. Holt (2002), Particle scale reservoir mechanics, *Oil & Gas Science and Technology - Rev. IFP*, **57**, 525–538.
- Liu, C. H., S. R. Nagel, D. A. Schecter, S. N. Coppersmith, S. Majumdar, O. Narayan, and T. A. Witten (1995), Force fluctuations in bead packs, *Science*, **269**, 513–515.
- Lockner, D. A., J. D. Byerlee, V. Kuksenko, A. Ponomarev, and A. Sidorin (1992), Observations of quasistatic fault growth from acoustic emissions, in *Fault Mechanics and Transport Properties of Rocks*, edited by B. Evans and T.-f. Wong, pp. 3–32, Academic Press, San Diego.
- Louis, L., T.-f. Wong, P. Baud, and S. Tembe (2006), Imaging strain localization by X-ray computed tomography: discrete compaction bands in Diemelstadt sandstone, *J. Struct. Geol.*, **28**, 762–775.
- Louis, L., P. Baud, and T.-f. Wong (2007), Characterization of pore-space heterogeneity in sandstone by X-ray computed tomography, in *Rock Physics and Geomechanics in the Study of Reservoirs and Repositories*, edited by C. David and M. Le Ravalec-Dupin, pp. 127–146, The Geological Society, Special Publications, **284**, London.
- Mair, K., I. G. Main, and S. C. Elphick (2000), Sequential development of deformation bands in the laboratory, *J. Struct. Geol.*, **22**, 25–42.
- Makse, H. A., D. L. Johnson, and L. Schwartz (2000), Force fluctuations in unconsolidated granular materials under uniaxial compression, *Phys. Rev. Lett.*, **84**, 4160–4163.
- Margolin, L. G., and B. C. Trent (1990), Towards a constitutive model for cemented granular materials, in *Rock Mechanics: Contributions and Challenges*, edited by W. A. Hustrulid and G. A. Johnson, pp. 321–328, A.A. Balkema, Rotterdam.
- Marketos, G., and M. D. Bolton (2005), Compaction bands as observed in DEM simulations, in *Powders and Grains*, edited by Garcia-Roja, Herrmann and McNamara, Taylor & Francis Group, London.
- Menéndez, B., W. Zhu, and T.-f. Wong (1996), Micromechanics of brittle faulting and cataclastic flow in Berea sandstone, *J. Struct. Geol.*, **18**, 1–16.
- Mollema, P. N., and M. A. Antonellini (1996), Compaction bands: A structural analog for anti-mode I cracks in aeolian sandstone, *Tectonophysics*, **267**, 209–228.
- Mora, P., and D. Place (1998), Numerical simulation of earthquake faults with gouge: Toward a comprehensive explanation for the heat flow paradox, *J. Geophys. Res.*, **103**, 21,067–21,089.
- Morgan, J. K., and M. S. Boettcher (1999), Numerical simulations of granular shear zones using the distinct element method. I. Shear zone kinematics and the micromechanics of localization, *J. Geophys. Res.*, **104**, 2703–2719.
- Olsson, W. A. (1999), Theoretical and experimental investigation of compaction bands in porous rock, *J. Geophys. Res.*, **104**, 7219–7228.
- Olsson, W. A., and D. J. Holcomb (2000), Compaction localization in porous rock, *Geophys. Res. Lett.*, **27**, 3537–3540.
- Potyondy, D. O., and P. A. Cundall (2004), A bonded-particle model for rock, *Int. J. Rock Mech. Min. Sci.*, **41**, 1329–1364.
- Potyondy, D. O., P. A. Cundall, and C. Lee (1996), Modeling rock using bonded assemblies of circular particles, *Proc. North Am. Rock Mech. Symp.*, **2**, 1937–1944.
- Radjai, F., M. Jean, J. J. M. O'reau, and S. Roux (1996), Force distributions in dense two-dimension granular systems, *Phys. Rev. Lett.*, **77**, 274–277.
- Rudnicki, J. W. (2004), Shear and compaction band formation on an elliptic yield cap, *J. Geophys. Res.*, **109**, B03402, doi:10.1029/2003JB002633.
- Sternlof, K. R., J. W. Rudnicki, and D. D. Pollard (2005), Anticrack-inclusion model for compaction bands in sandstone, *J. Geophys. Res.*, **110**, B11403, doi:10.1029/2005JB003764.
- Vajdova, V., P. Baud, and T.-f. Wong (2004a), Permeability evolution during localized deformation in Bentheim sandstone, *J. Geophys. Res.*, **109**, B10406, doi:10.1029/2003JB002942.

- Vajdova, V., P. Baud, and T.-f. Wong (2004b), Compaction, dilatancy and failure in porous carbonate rocks, *J. Geophys. Res.*, *109*, B05204, doi:10.1029/2003JB002508.
- Walton, K. (1987), The effective elastic moduli of a random packing of spheres, *J. Mech. Phys. Solid*, *35*, 213–226.
- Wang, B. S. (2003), *Numerical Research on Fracture Evolution in Granular Earth Material* (in Chinese), 99 pp, Ph.D. Thesis, University of Science and Technology of China, Hefei.
- Wong, T.-f., C. David, and W. Zhu (1997), The transition from brittle faulting to cataclastic flow in porous sandstones: Mechanical deformation, *J. Geophys. Res.*, *102*, 3009–3025.
- Wong, T.-f., P. Baud, and E. Klein (2001), Localized failure modes in a compactant porous rock, *Geophys. Res. Lett.*, *28*, 2521–2524.
- Wu, X. Y., P. Baud, and T.-f. Wong (2000), Micromechanics of compressive failure and spatial evolution of anisotropic damage in Darley Dale sandstone, *Int. J. Rock Mech. Min. Sci.*, *37*, 143–160.
- Zhang, J., T.-f. Wong, and D. M. Davis (1990), Micromechanics of pressure-induced grain crushing in porous rocks, *J. Geophys. Res.*, *95*, 341–352.
-
- Y. Chen and B. Wang, Institute of Geophysics, China Earthquake Administration, Beijing, 100081, China. (wangbs@cea-igp.ac.cn)
- T.-f. Wong, Department of Geosciences, Stony Brook University, NY 11794-2100, USA. (teng-fong.wong@stonybrook.edu)